JOURNAL OF MATERIALS SCIENCE 10 (1975) 2092–2111

Theories for the development of rolling textures in polyoxymethylene

M. J. MILES*, N. J. MILLS
Department of Physical Metallurgy and Science of Materials, University of Birmingham, Birmingham, UK

Two alternative models for the development of texture in rolled polyoxymethylene are developed. The first proposes that slip systems in the crystalline phase are the main deformation mechanisms, and calculates crystal rotations on the assumption of a uniform stress state in rolling. The second develops Wilchinsky's model of rigid crystals rotating in a deforming amorphous matrix. The former is shown to be in better agreement with experimental data.

1. Introduction

The crystalline texture (distribution of orientations) of uniaxially rolled polyoxymethylene (POM) has been investigated a number of times recently. Such texture is described by the orientation distribution of particular directions in the hexagonal unit cell of a crystal (such as the polymer chain direction [0 0 0 1] or the pole of a prismatic face such as [1 0 $\bar{1}$ 0]) with respect to the rolling direction R, the transverse direction T and the sheet normal N. In particular idealized components of the overall texture can be described in the form $\{1\,\bar{2}\,1\,0\}\langle 1\,0\,\bar{1}\,0\rangle$ which means that one of the set of $\{1\,\bar{2}\,1\,0\}$ planes is parallel to the sheet plane and one of the $\langle 1\,0\,\bar{1}\,0\rangle$ directions is parallel to R. Gezovich and Geil [1] rolled 3 mm thick injection moulded bars of POM and found that at 50% thickness reduction the main texture was of [0 0 0 1] at ± 30° to R in the RN plane and random $\langle 1\,0\,\bar{1}\,0\rangle$ poles about these positions, whereas at 70% thickness reduction the main element was a [0 0 0 1] fibre texture (the [0 0 0 1] axis along R but with [1 0 $\bar{1}$ 0] randomly spread in the NT plane). A major difference between this and later work was in the use of injection moulded bars, which have been shown to have a complex microstructure consisting of 0.1 mm of row nucleated skin with a nearly ideal [0 0 0 1] fibre texture, and only the central 1 mm of random spherulites, the intervening layers being of an intermediate transcrystalline nature [2]. Most other workers have used compression moulded sheet which should be entirely spherulitic. Starkweather *et al.* [3] found that for a 17% thickness reduction a $\{1\,\bar{2}\,1\,0\}\langle 1\,0\,\bar{1}\,0\rangle$ texture developed in POM sheet. Preedy and Wheeler [4] gave POM sheet a 60% thickness reduction at subambient temperatures and concluded that a phase change to a orthorhombic phase with a (1 0 0) [0 0 1] texture had occurred. Finally, Chang *et al.* [5] reduced POM sheet by 73% at 126° C by Steckel rolling and found a strong $\{1\,0\,\bar{1}\,0\}$ [0 0 0 1] texture.

Previous workers have disagreed over the deformation mechanisms that occur in the plastic deformation of POM. Gezovich and Geil [1] observed the [0 0 0 1] crystal axis tilted with respect to the surface of the lamellar crystals. However, slip on $\{1\,0\,\bar{1}\,0\}$ planes in the [0 0 0 1] direction was ruled out on the (erroneous) grounds that each $\{1\,0\,\bar{1}\,0\}$ plane must slip simultaneously by at least one c spacing of the unit cell and hence [0 0 0 1] would immediately rotate to within 12° of R. O'Leary and Geil [6] studied the tensile deformation of POM at 125° C, where spherulites were observed to deform into ellipsoidal shapes for up to 125% elongation. In zones of the spherulites where the twisted radial fibrils are roughly perpendicular to the tensile stress axis, these were observed to twist into tighter spirals

*Present address: Universitat des Saarlandes, Werkstoffphysik, 66 Saarbrucken, Germany.

until they fractured into segments, whereas fibrils within 30° of the tensile axis were undamaged. The roles of tie molecules in holding stacks of lamellar single crystals together in fibrils, and intercrystalline links between fibrils in holding different regions of a spherulite together were discussed. Starkweather *et al.* [3] suggested that, in spherulite fibrils parallel to R, [0 0 0 1] axes rotate to be parallel to T. However, this is hardly a detailed deformation mechanism, and no suggestions were made as to how other regions of the spherulites could attain the $\{1\,\bar{2}\,1\,0\}\langle 1\,0\,\bar{1}\,0\rangle$ texture. Chang *et al.* [5] concluded that at 126° C the single slip system $\{1\,0\,\bar{1}\,0\}$ [0 0 0 1] operates, i.e. slip occurs on $\{1\,0\,\bar{1}\,0\}$ planes in the [0 0 0 1] direction. The explanation for the crystal rotations is presumably that of Calnan and Clews [7] although with just a single type of slip system operating it is not clear how displacement continuity between crystals is preserved.

There is an extensive literature on texture development in rolled metals, but as yet no comprehensive theory. To overcome the problem of the unknown interactions between crystals in a deforming polycrystalline material, it is usual to simplify the situation by assuming either a uniform state of stress, or of strain, throughout the material. The assumption implies discontinuous strains or stresses respectively at the crystal boundaries. Von Mises [8] established that there must be five independent slip systems in a crystal for an arbitary change of shape to be possible. Further, for a single crystal slipping on a single system, the rotations of the crystal lattice are established for two experimental situations: (1) in a tensile test on a long thin crystal the constraint that the grips remain on the tensile axis causes the slip direction to rotate towards that tensile axis, (2) in a uniaxial compression test, the constraint that the platen surfaces remain normal to the axis of compression causes the slip plane normal to rotate towards that axis [9].

In Calnan and Clews' [7] treatment of rolling textures, uniform stress conditions were assumed only to apply to crystals near the sheet surface. They assumed that the crystals would rotate in the same manner as constrained single crystals, and by comparing the predicted stable textures for uniaxial tension along the rolling direction, and for uniaxial compression along the sheet normal direction deduced that those textural components occuring in both would be stable in rolling. Dillamore and Roberts [10] assumed a uniform state of stress throughout the sheet, and calculated the resolved shear stresses on the slip systems in b c c and f c c metals for the simultaneous application of a tensile stress along R and an equal compressive stress along N. They assumed that slip on the system with the highest resolved shear stress would cause the slip direction to rotate towards R and simultaneously the slip plane normal towards N. Such theories can only be checked by comparing the predicted stable textures with those of metals rolled to say 1% of the original thickness. To allow comparisons at moderate reductions, Leffers [11] developed a computer program based on Dillamore and Robberts' approach. In it each f c c crystal shears by increments of 0.05 shear strain on the $\{1\,1\,1\}\langle 1\,1\,0\rangle$ slip system with the highest resolved shear stress. He was able to predict typical pole figures for rolled brass. The opposite approach of assuming uniform strain throughout the polycrystalline aggregate has been used by Kallend and Davies [12] for f c c metals. They used the Bishop and Hill [13] principle of maximum work to determine which of the many possible sets of slip systems were operative, and made further assumptions to allocate the total shear among the slip systems. Their results suggest that $\{1\,1\,1\}\langle 1\,1\,0\rangle$ slip systems lead to a pure copper rolling texture, whereas to obtain a typical brass rolling texture, deformation twinning is also required. Thus there are two quite different computer models, one based on uniform stress and the other on uniform strain, that can be used to explain the rolling textures of f c c metals.

Hammer *et al.* [14] found POM to be a material with approximately 75% crystallinity by weight, and a complex spherulitic microstructure, so most models for the deformation of POM are gross simplifications. One extreme is to treat the deformation as occuring entirely in the amorphous matrix so that the crystals rotate but are not plastically strained. Wilchinsky [15] has proposed two such models and he has calculated the average c axis orientation for a plane strain deformation. This model has been to some extent confirmed by Hay and Keller's [16] observations on two dimensional ringed polyethylene spherulites and given support by Wang's [17] analysis of the elastic anisotropy of polyethylene spherulites. The other extreme is to treat POM as a polycrystalline material; so that all the plastic deformation occurs in the crystals. We have investigated the value of

both the polycrystalline approximation and Wilchinsky's model in the prediction of the rolling texture of POM.

2. Observed crystal deformation mechanisms

Bassett [18] has examined single crystals of POM in the electron microscope. The polymer forms hexagonal plate like crystals with (0 0 0 1) surfaces and $\{1\,0\,\bar{1}\,0\}$ growth planes. By observing Moiré fringes between bilayer crystals having a slight relative rotations, dislocations were identified having a horizontal component of Burgers vector of $a/3\langle 1\,1\,\bar{2}\,0\rangle$ which is the shortest lattice translation. Such dislocations can only move easily without breaking covalent bonds by moving in the closest packed $\{1\,0\,\bar{1}\,0\}$ fold planes. This suggests $\{1\,0\,\bar{1}\,0\}\langle 1\,1\,\bar{2}\,0\rangle$ as a possible slip system. Garber and Geil [19] observed the deformation of POM single crystals on a "Mylar" film and found that at 90% tensile strain slip occurs on $\{1\,0\,\bar{1}\,0\}$ planes in $\langle 1\,\bar{2}\,1\,0\rangle$ directions, with straight slip lines crossing the boundaries of sectors having different fold plane directions. Bassett [18] was unable to determine the c component of any Burgers vector, so there is no direct evidence for the $\{1\,0\,\bar{1}\,0\}$ [0 0 0 1] slip system.

Young *et al.* [20] have analysed the slip system in certain plane strain deformations of highly oriented high-density polyethylene. They concluded that chain slip would cause the [0 0 1] direction to rotate towards R and the lamellar surface normals to rotate towards N. In POM $\{1\,0\,\bar{1}\,0\}$ [0 0 0 1] is the equivalent of chain slip, so applying this analysis to Gezovich and Geil's [1] wide-angle and small-angle X ray data leads to the conclusion that chain slip occurs in the rolling of POM. Young *et al.* also found that elastically recoverable shear strains of about 0.3 could occur in the amorphous interlamellar material.

To find out whether there are five independent slip systems in POM the tensor strain ($\epsilon_{ij} = \frac{1}{2}(\partial u_i/\partial x_j + \partial u_j/\partial x_i)$, where u is the displacement and x the position co-ordinate, was calculated for each of the slip systems so far mentioned. The 1, 2 and 3 axes were taken along $[1\,0\,\bar{1}\,0]$, $[1\,2\,\bar{1}\,0]$ and [0 0 0 1] respectively. Table I shows that there are four independent slip systems (only four sets of ϵ_{ij} cannot be formed by combinations of other sets), and in particular there is no tensile or compressive strain in the [0 0 0 1] direction. In hexagonal metals there is usually at least one twinning deformation that compresses [0 0 0 1] and one that extends it, but there is no experimental evidence for deformation twinning in POM. However, interlamellar shear could provide an ϵ_{33} component so long as the lamellar normal is not along the [0 0 0 1] direction. If the surfaces of the lamellar crystals are initially (0 0 0 1) planes, this implies that interlamellar shear can provide the fifth independent slip system so long as some $\{1\,0\,\bar{1}\,0\}$ [0 0 0 1] slip has already taken place.

Since any slip system would presumably operate by dislocation movement, it is necessary to consider the strain field energy of such dislocations, especially in the case of $\{1\,0\,\bar{1}\,0\}$ [0 0 0 1] slip where the Burgers vector could be 17.3 Å. Schultz [21] has discussed the results of Eshelby and Stroh [22] who showed that the strain field energy of a screw dislocation passing through a thin plate-like crystal was far less than that of a similar dislocation in a massive crystal. Allowing also for the low shear modulus of polymer crystals, Schultz showed that the strain field energy of a screw dislocation of $b = 2.5$ Å passing through a polyethylene crystal of thickness 100 Å would only be ~ 1 eV, a value low enough to conceive of thermal generation of such dislocations at room temperature. It is possible that a dislocation of Burgers vector 17.3 Å would split into partial dislocations, to reduce its strain energy.

Finally, there is the possibility of inhomogeneous deformation or micronecking. Hammer *et al.* [14] observed micronecking in the extension of large two-dimensional POM spherulites and Garber and Geil [17] observed fibrillation in cracks in deformed single crystals. In contrast with the

TABLE I Crystal strain components for unit shear strains on POM slip systems

	Slip system	ϵ_{11}	ϵ_{22}	ϵ_{33}	ϵ_{12}	ϵ_{23}	ϵ_{31}
1	$(1\,0\,\bar{1}\,0)$ [0 0 0 1]	0	0	0	0	0	0.5
2	$(0\,1\,\bar{1}\,0)$ [0 0 0 1]	0	0	0	0	$0.25\sqrt{3}$	0.25
3	$(\bar{1}\,1\,0\,0)$ [0 0 0 1]	0	0	0	0	$0.25\sqrt{3}$	−0.25
4	$(1\,0\,\bar{1}\,0)$ $[\bar{1}\,2\,\bar{1}\,0]$	0	0	0	0.5	0	0
5	$(0\,1\,\bar{1}\,0)$ $[\bar{2}\,1\,1\,0]$	$-0.25\sqrt{3}$	$0.25\sqrt{3}$	0	−0.25	0	0
6	$(\bar{1}\,1\,0\,0)$ $[\bar{1}\,\bar{1}\,2\,0]$	$0.25\sqrt{3}$	$-0.25\sqrt{3}$	0	−0.25	0	0

plane stress conditions in these studies, such micronecking in bulk POM would involve simultaneous cavitation (in the same way as craze formation does in glassy polymers) and hence would be less likely to occur.

3. Uniform stress crystal slip model of uniaxial rolling texture development

A uniform stress model was chosen since there is evidence that the plastic strain in deformed spherulites is inhomogeneous, and because the computation is easier. The difficulty with attempting a uniform strain model is that the necessary interlamellar shear occurs on a plane that is ill-defined in terms of the crystal axes, so that the calculation of crystal rotations would depend on many further assumptions. The amorphous material is assigned an important role in the uniform stress model, for as well as providing a means of c-axis extension in the "crystal" composed of a stack of lamellae with amorphous interlayers, it must accommodate strain discontinuities at "crystal" boundaries, and transmit the uniform stress to the crystals.

3.1. Resolved shear stress for a crystal of arbitary orientation

Rowe [23] has analysed the stress conditions in the rolling process treating it as a plane strain deformation process in the RN plane. The R, T and N axes are principal stress axes, if the frictional forces on the sheet surface are low. The deformation is assumed to be homogeneous, so, if the material obeys the Von Mises yield criterion, the relevant Levy–Von Mises equation

$$d\epsilon_T = \lambda[\sigma_T - \tfrac{1}{2}(\sigma_R + \sigma_N)]$$

predicts that the principal stress in the T direction $\sigma_T = \frac{1}{2}(\sigma_R + \sigma_N)$ since the plastic strain increment in the T direction $d\epsilon_T = 0$. The stress tensor in the RTN axes can, therefore, be split into a dilational part, which increases in magnitude towards the centre of the roll nip as a result of the "friction hill", and a deviatoric part which may be written

$$\boldsymbol{\sigma} = \begin{pmatrix} K & 0 & 0 \\ 0 & 0 & 0 \\ 0 & 0 & -K \end{pmatrix}$$

where K is a constant stress $= \frac{1}{2}(\sigma_R - \sigma_N)$. Since the plastic deformation processes are assumed to occur at a critical resolved shear stress, only the deviatoric stress tensor is of interest. For this purpose, therefore, the stress system in rolling may be treated as being equivalent to a tensile stress K along R, and a compressive stress $-K$ along N.

We have observed that isotropic POM appears to obey the Von Mises yield criterion modified to include a small dependence on the dilational stress component. After being rolled the polymer eventually becomes anisotropic in its yielding behaviour, and the yield stress for a particular type of plastic strain depends on the sign of the plastic strain increment. Thus the stress analysis may only be expected to apply for the initial stages of rolling reduction.

It is assumed that the deviatoric stress tensor acts equally on all the crystals in the polymer. In order to calculate the resolved shear stresses on the various slip systems the stress tensor must be transformed into individual crystal axes from the RTN axes. The RTN axes may be rotated into the crystallographic 123 axes ($1 = 1\,0\,\bar{1}\,0$, $2 = \bar{1}\,2\,\bar{1}\,0$, $3 = 0\,0\,0\,1$) as follows (see Fig. 1):

(1) rotate RTN about $0N$ by α anticlockwise to $R'T'N$;

(2) rotate $R'T'N$ about $0R'$ by β anticlockwise to $R'T''3$;

(3) rotate $R'T''3$ about 03 by γ anticlockwise to

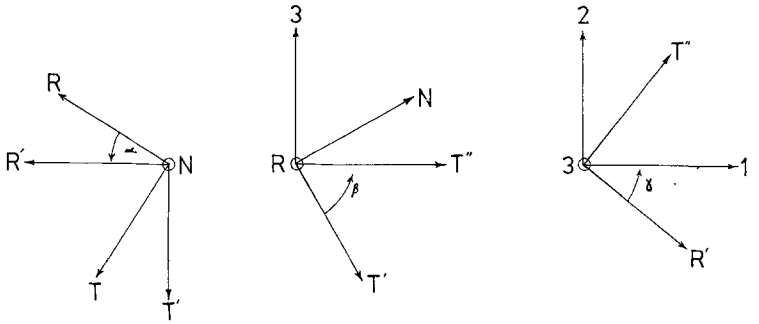

Figure 1 Euler angle rotations, carried out in sequence to transform RTN axes to 123 axes.

123.

The position of each crystal is thus defined by the Euler angles α, β, γ. In the 123 axes the deviatoric stress sensor becomes

$$\boldsymbol{\sigma}' = \mathbf{R}\boldsymbol{\sigma}\mathbf{R}^T$$

where $\mathbf{R}$ is the rotation matrix:

$$\begin{pmatrix} \cos\alpha\cos\gamma - \sin\alpha\cos\beta\sin\gamma & \sin\alpha\cos\gamma + \cos\alpha\cos\beta\sin\gamma & \sin\beta\sin\gamma \\ -\cos\alpha\sin\gamma - \sin\alpha\cos\beta\cos\gamma & -\sin\alpha\sin\gamma + \cos\alpha\cos\beta\cos\gamma & \sin\beta\cos\gamma \\ \sin\alpha\sin\beta & -\cos\alpha\sin\beta & \cos\beta \end{pmatrix}$$

and $\mathbf{R}^T$ its transpose. The resolved shear stress for the slip system $(1\,0\,\bar{1}\,0)$ $[0\,0\,0\,1]$ (system 1 of Table I) is

$$\sigma'_{13} = \tfrac{1}{2}K\sin 2\alpha\sin\beta\cos\gamma - \tfrac{1}{2}K(\sin^2\alpha + 1)\sin 2\beta\sin\gamma.$$

For slip systems 2 and 3, $\gamma + \pi/3$ and $\gamma + 2\pi/3$ can be substituted for γ in the above equation. For the slip system $(1\,0\,\bar{1}\,0)$ $[\bar{1}\,2\,\bar{1}\,0]$ (system 4 of Table I) the resolved shear stress is

$$\sigma'_{12} = \tfrac{1}{2}K(\sin^2\alpha\cos^2\beta - \cos^2\alpha - \sin^2\beta)\sin 2\gamma - \tfrac{1}{4}K\sin 2\alpha\cos\beta\cos 2\gamma.$$

By replacing γ by $\gamma + \pi/3$ and $\gamma + 2\pi/3$ in the above equation, the resolved shear stresses for slip systems 5 and 6, respectively, may be calculated.

3.2. Active slip systems

There is no evidence for polymer systems to suggest whether crystals largely slip on a single system, or whether many slip systems are simultaneously activated. Nor, at least for POM, have plasticity measurements been made on single crystals (or singly textured material) to determine the critical resolved shear stresses for the slip systems. In polyethylene at least Young *et al.* [20] have provided evidence that the Schmid law of a critical resolved shear stress for $[0\,0\,1]$ slip applies. Thus for POM we assume that each crystal slips solely on the system for which the critical resolved shear stress is first exceeded. Symmetry dictates that slip systems 1, 2, or 3 (chain slip) have the same critical resolved shear stress, as do systems 4, 5 or 6 (prismatic slip). At present, however, we must weight the resolved shear stress for chain slip by an arbitarily chosen constant (A) in determining the active system.

Another problem is to determine the amount of shear (S) on the active slip system. The largest resolved shear stress will vary with the orientation of the crystal, and relationship between the plastic shear strain and the resolved shear stress is unknown. We have assumed, as Leffers [11] did, that the increment of S is the same for all crystal orientations. The value chosen, 0.1, is a compromise between determining precisely the point at which the active slip system changes, and the computation time.

3.3. Crystal rotations on slip

In the absence of any other simple constraints, we have assumed, as did Leffers, that the crystals are constrained as follows.

(a) A material line lying along the R direction before slip must retain this orientation after slip.

(b) A plane of material with its pole in the N direction before slip must retain this orientation after slip.

These constraints are those appropriate to a single crystal in a uniaxial tension or compression test. It is difficult to express physically the shape constraints of neighbouring crystals in a polycrystal that would give rise to them. Once these constraints are established, then the rotations of the crystal axes relative to RTN is found by the methods of Kelly and Groves [9]. These give, for a crystal with its crystallographic axes fixed in space, the new position of any imbedded material line or plane after single slip by a shear strain S. The new set of Euler angles representing the crystal orientation after shear may be obtained from the rotated positions R' of the rolling direction and N' of the compression direction in the crystallographic axes.

3.4. Computation of the pole figures

A program was written in FORTRAN IV which consisted of the following stages.

(1) 99 sets of Euler angles were read in to represent the initial crystal orientations. Wunderlich [24] describes the polyoxymethylene crystal as belonging to the trigonal crystal system and having a $P3_1$ space group. As the lattice is hexagonal we have ignored the details of the intermolecular forces in the crystal and assumed that both the crystal and its slip systems have hexagonal

symmetry. Accordingly the Euler angles were restricted to the following ranges

$\Pi/2 > \alpha > -\Pi/2$ since in the pole figure recovery the distance of any pole from both the positive and negative R axis is used.

$\Pi/2 > \beta > 0$ since the crystal has mirror symmetry about (0 0 0 1).

$\Pi/3 > \gamma > 0$ since the crystal 0 0 0 1 axis is a six-fold symmetry axis.

Eleven pairs of β and γ were chosen to give positions of N roughly equally spaced at 0.35 radian intervals in the twelfth part of the spherical surface between the (0 0 0 1), (1 0 $\bar{1}$ 0) and ($\bar{1}$ 1 0 0) planes, and for each pair nine values of α at 0.35 radian intervals were used. It was checked that if the pole figure recovery process (step 9) was used on the initial sets of Euler angles, the polefigures had an approximately uniform pole density.

(2) For successive runs the constant A was given the value 0.5, 1, 1.5, and 2. For each crystal the slip system with the largest numerical value of A times the resolved shear stress for chain slip, or resolved shear stress for prism slip, was determined. The shear strain increment S on this system was assigned the value of 0.1 times the sign of the resolved shear stress.

(3) The angles λ_R and λ_N between the slip direction and the R and N axes respectively, and ϕ_R and ϕ_N between the pole of the slip plane and R or N were calculated from the Euler angles using relationships specific to each slip system. Appendix 1 gives details.

(4) The relationships derived by Kelly and Groves [9] were used to find the new values of λ and ϕ after slip, L the extension ratio of a material line initially along R, and r the ratio of the final to initial separation of any two material planes that stay parallel to the RT plane.

$$L^2 = 1 + 2S\cos\phi_R\cos\lambda_R + S^2\cos^2\phi_R$$

$$1/r^2 = 1 - 2S\cos\phi_N\cos\lambda_N + S^2\cos^2\lambda_N$$

$$\sin\lambda_R/\sin\lambda'_R = \cos\phi_R/\cos\phi'_R = L$$

$$\cos\lambda'_N/\cos\lambda_N = \sin\phi'_N/\sin\phi_N = r.$$

Note that we have assumed S to be positive in the first two equations.

(5) Relationships specific to each slip system were used to recover the new values of α, β and γ that specify the crystal orientation after shear. Appendix 1 gives details.

(6) After n increments of shear strain in all the crystals the products $r_1r_2r_3 \ldots r_n$ and $L_1L_2L_3 \ldots L_n$ were computed for each crystal r_n and L_n being respectively the value of r and L for the nth strain increment. The average values

$$\bar{r} = \overline{r_1r_2 \ldots r_n}$$

and

$$\bar{L} = \overline{L_1L_2 \ldots L_n}$$

were calculated. Assuming that there was no volume change on deformation the average width $\bar{w}$ of the sheet was calculated using

$$\bar{w}\bar{r}\bar{L} = 1.$$

(7) If $\bar{r}$ was approximately 0.7, 0.5 or 0.3 then step 8 was carried out. If not, a further increment of shear strain was imposed on all the crystals by returning to step 2.

(8) The crystal positions relative to the RTN axes were recovered and displayed as pole figures for comparison with experimental data. Each crystal contributes one (0 0 0 1) pole, or three {1 0 $\bar{1}$ 0} poles, or six {1 0 $\bar{1}$ 5} poles to the stereographic projection of the respective pole figure. Pole figures centred on N were produced. Since these must have mirror symmetry about the NT and NR planes only one quadrant was displayed. The angular distances of all the poles of a particular type from N were calculated, and those more than $\Pi/2$ away rejected. For the remaining poles the angular distances from both the positive and negative R axis were calculated and the value less than $\Pi/2$ used. Finally, the co-ordinates of the poles in the fourth quadrant of the pole figure were calculated from the angular distances from N and R (Appendix 2 gives details). Computer graph plots of the pole figures were obtained using the University's I.C.L. 1960A computer.

3.5. Results of computation

The computed pole figures are compared with experimental results in a later section. The main features of the computed pole figures are described here, and the main crystal deformation mechanisms outlined. It was found that the best correspondence between theoretical and experimental pole figures occurred when the constant $A = 1.5$, i.e. the critical resolved shear stress for slip on {1 0 $\bar{1}$ 0} planes in the [0 0 0 1] direction is only 2/3 of that for slip on the same planes in ⟨1 $\bar{2}$ 1 0⟩ directions. The following description applies for $A = 1.5$.

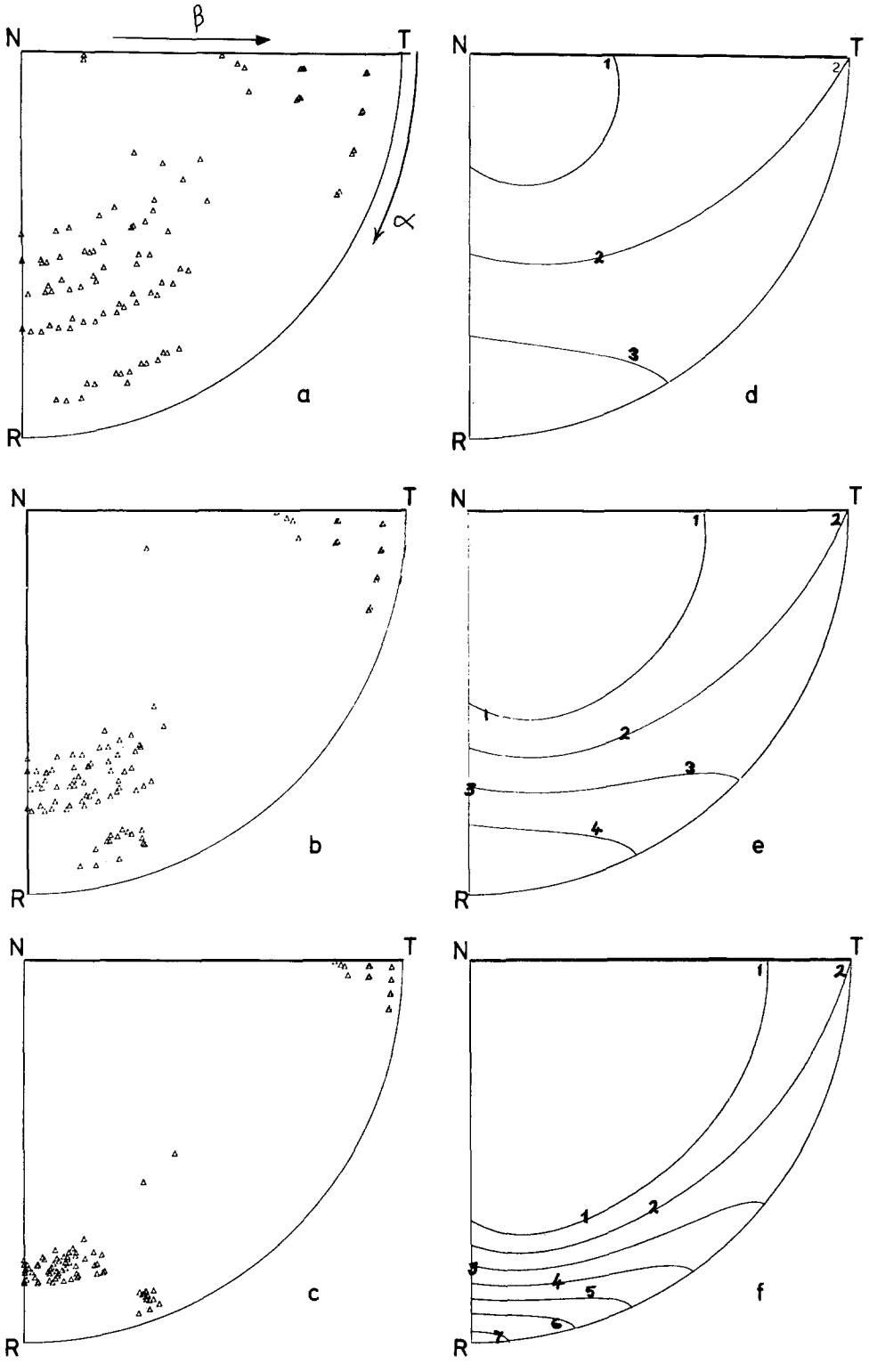

Figure 2 Stereographic projections of 0 0 0 1 pole figures for uniaxially rolled POM (a), (b) and (c) are from the crystal slip theory after total shears of 1.0, 2.0, and 3.8 per crystal; (d), (e) and (f) are contours of pole intensity for the Wilchinsky model. Contour level 1 is $\frac{1}{2}$ the undeformed random level, 2 is random, 3 is twice random, etc. (a) and (d) are for $r = 0.7$, (b) and (e) are for $r = 0.5$, (c) and (f) are for $r = 0.3$.

Fig. 2 shows that the 22% of the crystals, that initially had their 0 0 0 1 axis within ~ 40° of T, rotate their 0 0 0 1 axis towards T, and Fig. 8b shows that even at a reduction of $\bar{r} = 0.7$ the corresponding $1\,0\,\bar{1}\,0$ poles have begun to peak in the RT plane and at 30° from N. Examination of the sequence of active slip systems shows that these crystals all undergo prism (or $\{1\,0\,\bar{1}\,0\}$ $\langle\bar{1}\,2\,\bar{1}\,0\rangle$) slip, and after a maximum of twelve strain increments ($\bar{r} = 0.66$) this changes to duplex prism slip on pairs of systems such as

-5 and 6 i.e. $(0\,1\,\bar{1}\,0)\,[2\,\bar{1}\,\bar{1}\,0]$ and

$(\bar{1}\,1\,0\,0)\,[\bar{1}\,\bar{1}\,2\,0]$

or

-4 and 5 i.e. $(1\,0\,\bar{1}\,0)\,[1\,\bar{2}\,1\,0]$ abd

$(0\,1\,\bar{1}\,0)\,[\bar{2}\,1\,1\,0]$.

Such duplex slip then continues and eventually the stable $\{\bar{1}\,2\,\bar{1}\,0\}\langle 1\,0\,\bar{1}\,0\rangle$ texture is reached. Fig. 3 shows the operation of these forms of duplex slip in the stable position.

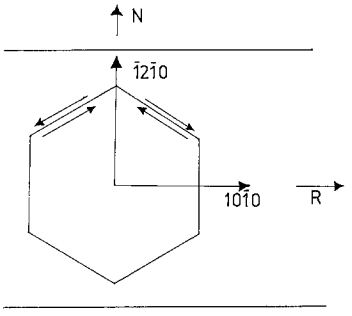

Figure 3 A typical position of a crystal's axes relative to the sheet axes after duplex prism slip.

Fig. 2 shows that the remaining 78% of the crystals rotate their 0 0 0 1 axes towards R, and that the rate of rotation slows down as they approach R. They undergo chain (or $\{1\,0\,\bar{1}\,0\}$ [0 0 0 1]) slip on a single slip system. There is little tendency for the slip plane normals to cluster at N in the $1\,0\,\bar{1}\,0$ pole figure, until $\bar{r} \sim 0.2$. However, there is a boundary between chain and prism slip that occurs when the 0 0 0 1 axis is on an arc that extends roughly from 10° from R in the RN plane to 20° from R in the RT plane. The exact boundary also depends on the orientation of the $1\,0\,\bar{1}\,0$ poles, so it cannot be drawn as a curve in the 0 0 0 1 pole figure. When a 0 0 0 1 pole reaches this boundary, the crystal then either undergoes prism slip, or a complex mixture of prism and chain slip. The eventual stable orientation is only reached when $\bar{r} < 0.2$, which is beyond the experimental reduction limit. The stable orientation is of a $\{1\,\bar{2}\,1\,0\}$ plane in the sheet plane, and the 0 0 0 1 pole in the RT plane but at 20° from R.

3.6. Macroscopic stresses and strains in the rolling process

The change in the overall sheet dimensions as rolling proceeds are predicted in Fig. 4. It is encouraging to see that the sheet width is predicted to stay reasonably constant. Thus the deformation process postulated is not inconsistent with the plane strain nature of the rolling process.

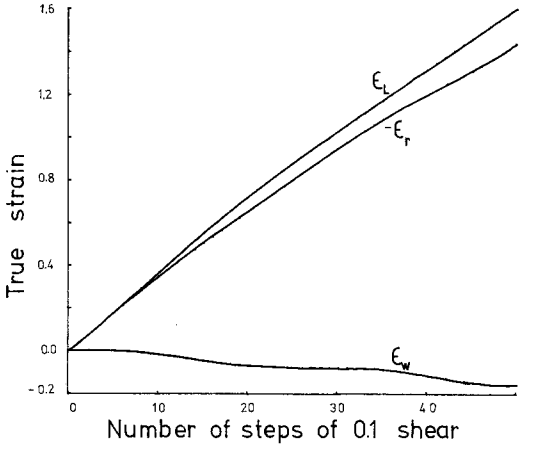

Figure 4 Macroscopic principal true strains predicted by the crystal slip model as a function of the total shear strain per crystal. The suffices L, r and w refer to the length in the rolling direction, the reduction in thickness, and the width, respectively.

In order to find the approximate degree of orientation hardening in the polymer as the crystal texture changes, after each shear strain increment the average value for all crystals of the reciprocal of the magnitude of the resolved shear stress on the active system was calculated. Whether this is the correct average to take is debatable, but it seems consistent with the assumption that each crystal undergoes the same shear increment. Since in this calculation the resolved shear stresses have been weighted by the factor A, the result, shown in Fig. 5, may be interpreted as the ratio of effective stress magnitude K in rolling to the critical resolved shear stress for prism slip. Since, however, this latter quantity is unknown at present, only the rate of increase in K with rolling reduction can be compared with experimental data. Fig. 5 shows that the experimental orientation hardening is greater than that predicted by

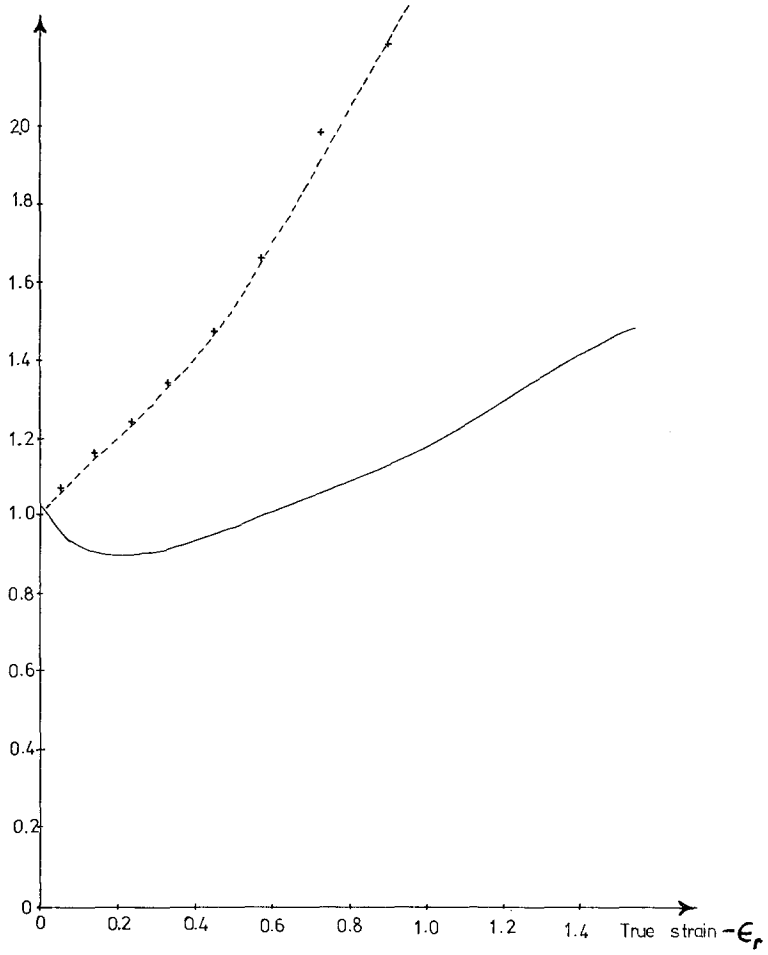

Figure 5 Macroscopic true stresses predicted by the crystal slip model as a function of the true strain ($-\epsilon_r$). The solid line is the predicted yield stress, K, of the slip model divided by the initial value. The dashed line is experimental data for the plane strain compression of POM at 20° C and strain rate 0.01 min^{-1}, again normalized with respect to the initial compressive yield stress.

the crystal slip model. This is not surprising since other mechanisms such as dislocation–dislocation interactions or orientation hardening in the amorphous phase could also contribute to the effect.

3.7. Uniform stress crystal slip model for biaxial rolling

By making minor modifications in the uniaxial rolling computer program, it was possible to simulate the effect of alternate small rolling reductions of a sheet in two perpendicular directions, R_1 and R_2.

If the shear increment number was odd, then after step 5 of Section 3.4 the new value of α was increased by $\pi/2$. For odd shear increments the Euler angles define the sheet axes R_1R_2N with respect to the crystal. For even shear increments the position of N, defined by β and γ, is unchanged, but R_1 replaces R_2 and R_2 replaces $-R_1$.

$\bar{L}$ is redefined as

$$\bar{L} = \overline{\frac{L_1}{r_2L_2}\frac{L_3}{r_4L_4}\cdots\frac{L_{2n-1}}{r_{2n}L_{2n}}}$$

and the pole figures are only recovered after an even number of shear increments.

Examination of the computed 0001 pole figures in Fig. 6 show that 28 of the poles move towards each of R_1 and R_2 and the remaining 43 move towards a position midway between R_1 and R_2 and 80° from N. The latter are always undergoing chain slip (for instance alternatively on systems -1 and -3), but this position to which the 0001 axis moves is not a stable end position – eventually for $\bar{r} < 0.2$ the number of poles at this position declines. The former 0001 poles

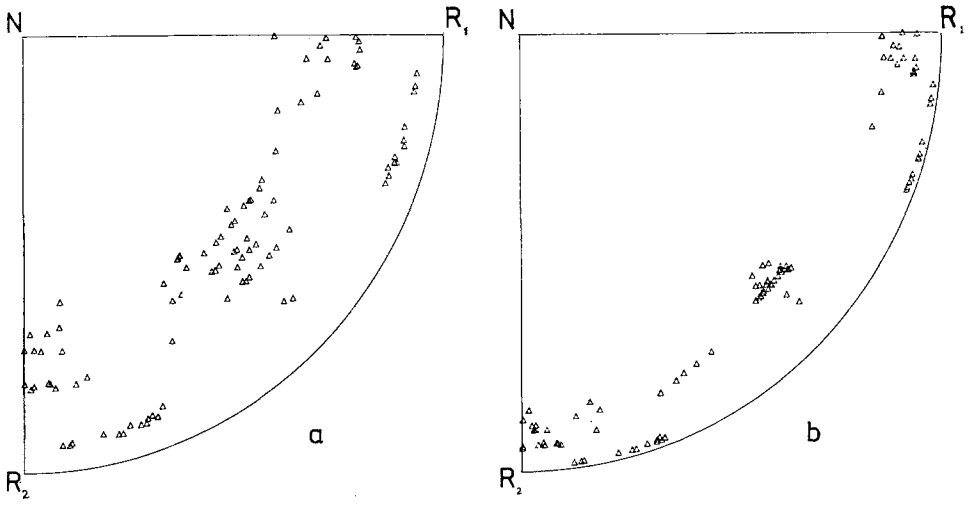

Figure 6 0 0 0 1 pole figures for equally biaxially rolled POM predicted by the crystal slip model. a and b are after total shears of 2.0 and 5.4, for which $r = 0.504$ and 0.207 respectively.

eventually reach the R_1R_2 plane and are within about $\pm 20^\circ$ of R_1 or R_2. In this stable state they undergo duplex slip on prism slip systems -4 and 5 or -5 and 6 exactly as was found in the uniaxial rolling model. The important feature of the biaxial rolling model is, therefore, that the majority of the crystals end up on a position where duplex prism slip operates with a $\{1\,\bar{2}\,1\,0\}$ plane in the plane of the sheet, and the [0 0 0 1] axis within 20° of either R_1 or R_2, whereas the minority go through an intermediate texture described by ($\alpha = 45^\circ$, $\beta = 80^\circ$, γ random). The sharpness of this latter texture will depend on the rolling reductions in the R_1 and R_2 directions being exactly equal, a condition that is unlikely to be met in practice.

4. Wilchinsky's model applied to uniaxial rolling textures

The simpler of Wilchinsky's [15] two models is one in which a viscous matrix causes imbedded rigid crystals to rotate without deforming when the matrix is deformed. Some interaction between the crystals, such as the interlamellar tie molecules, causes the crystal c-axis orientation to change. More specifically a crystal c-axis changes its orientation by exactly the same amount as would a parallel embedded material line in a homogeneously deformed solid. This presumably implies that the extensible tie-molecules (or other means of interaction) are the main stress bearing component of the microstructure. However implausible the mechanism may be, what is really being tested is the assumed constraint on the crystals in deformation.

The orientation of the c-axis of a crystal in the undeformed material can be described by the R, T and N direction components of unit vector along c. In the rolled material these components are multiplied by $1/r$, 1 and r respectively, where r is the reduction in sheet thickness. Wilchinsky only calculated the average value of $\cos^2$ (the angle between the c-axis and R) for an initially uniform distribution of c-axes. However, using the computer program of Section 3.4, it is a simple modification to calculate any pole figure of a set of crystals rotating according to Wilchinsky's assumed constraints. In a 0 0 0 1 pole figure such as Fig. 2 the position of a pole is defined by the Euler angles α and β. In terms of the initial Euler angles, the RTN components of a vector representing the c-axis orientation are $[(1/r)\sin\alpha\sin\beta, \cos\alpha\sin\beta, r\cos\beta]$ after rolling. Thus the new Euler angles $\alpha'\beta'\gamma'$ are

$$\alpha' = \tan^{-1}(\tan\alpha/r)$$

$$\beta' = \tan^{-1}(\tan\beta\sqrt{(\sin^2\alpha + r^2\cos^2\alpha)}/r^2)$$

$$\gamma' = \gamma.$$

This reorientation was applied for the cases $r = 0.5$ and 0.3 to the set of 99 crystals described in Section 2.2.4, and the 0 0 0 1, 1 0 $\bar{1}$ 0 and 1 0 $\bar{1}$ 5 pole figures calculated. Contour levels of pole intensity were also computed from the continuous 0 0 0 1 pole intensity function. If this function is unity in the undeformed material, then the intensity $I(\alpha', \beta')$ in the deformed material may be found from the conservation of the number of

poles in a small solid angle $\sin\beta\, d\alpha\, d\beta$ which becomes $\sin\beta' d\alpha' d\beta'$ on deformation, i.e. $I = \sin\beta\, d\alpha\, d\beta / \sin\beta' d\alpha' d\beta'$. Use of the expressions for the transformation of Euler angles leads to the result

$$I = \frac{r^3 [4w - \sin 2\alpha' \sin 2\beta' (1 - r^2)]}{4w[1 - \sin^2 \beta' (1 - r^2 w)]^{3/2}}$$

where $w = r^2 \sin^2 \alpha' + \cos^2 \alpha'$. Recourse was then made to a computer contour program that drew contour levels in the 0 0 0 1 pole figure from the values of I calculated on a square 45 x 45 array of points. The intensity contours may be compared with the discrete pole distribution, giving a useful cross check on the calculations. The 0 0 0 1 pole intensity varies smoothly, with a single maximum of $1/r^3$ at R, unit intensity at T, and a minimum of r^3 at N (Fig. 2).

Since the third Euler angle γ is supposed to remain randomly distributed in the Wilchinsky model, the $1\,0\,\bar{1}\,0$ pole figure intensity may be calculated as the average 0 0 0 1 intensity at points on a great circle at $\Pi/2$ from the point concerned. The 0 0 0 1 pole figure has mirror planes perpendicular to R and T, so the $1\,0\,\bar{1}\,0$ intensity was calculated from the 0 0 0 1 intensity at 20 points equally spaced around one half of the great circle. The results in Figs. 8c. 9c and 10c show a broad intensity band from N to T with the maximum intensity at N. This maximum is weaker than that in the corresponding 0 0 0 1 pole figure.

The $1\,0\,\bar{1}\,5$ pole figure intensity may be calculated in a similar way as the average 0 0 0 1 intensity around a small circle of radius 42° from the $1\,0\,\bar{1}\,5$ position of interest. The results in Figs. 9f and 10f show that there are fewer contours than in the corresponding $1\,0\,\bar{1}\,0$ pole figures, and that it is not until $r = 0.3$ that any distinct texture emerges.

The Winchinsky model can also be applied to equal biaxial rolling, since the overall strains are the same as those for uniaxial compression. If the reductions in sheet thickness is r, then only the second Euler angle β is changed by the deformation process. The value β' in the deformed material is given by

$$r\sqrt{r} \tan\beta' = \tan\beta.$$

Consequently, the 0 0 0 1 pole figure has axial symmetry about N, the intensity being given by $I = [r/\cos\beta' \sqrt{(1 + r^3 \tan^2 \beta')}]^3$. Fig. 7 shows that the 0 0 0 1 intensity increases from r^3 at N to $1/r\sqrt{r}$ at 90° from N. The $1\,0\,\bar{1}\,0$ and $1\,0\,\bar{1}\,5$ pole figures also have axial symmetry about N, and are obtained by averaging the 0 0 0 1 intensity around a circle of radius 90° and 42° respectively centred on the value of β' of interest.

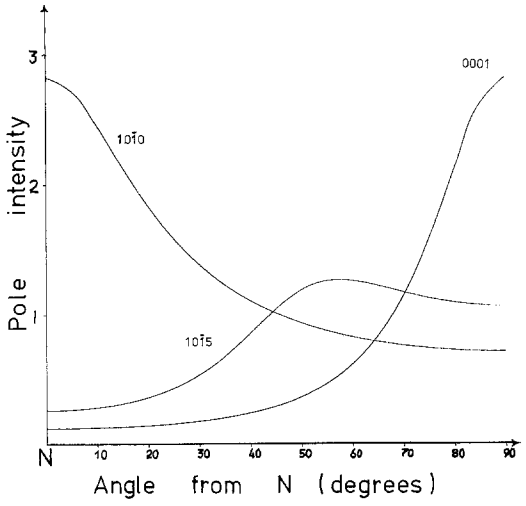

Figure 7 Pole intensity as a function of the angular distance from N for the 0 0 0 1, $1\,0\,\bar{1}\,0$ and $1\,0\,\bar{1}\,5$ pole figures for equally biaxially rolled POM predicted by the Wilchinsky model for $r = 0.5$.

5. Sample preparation

A high molecular weight I.C.I. "Kematal" polyoxymethylene copolymer (Melt Flow Index 2.5 at 190° C) was used. Granules were compression moulded at 200° C into 150 mm x 150 mm sheets which were rapidly cooled. These were uniaxially rolled at 20° C at a rate of 25 mm sec^{-1} with a reduction of about 0.03 mm per pass to a final thickness of 0.8 mm, the direction of rolling being reversed at each pass. By using various initial sheet thicknesses a variety of thickness reductions were achieved. Excessive temperature rises were avoided, and the deformation was effectively plane strain, with negligible width increase in the transverse direction.

5.1. Preparation of X-ray figures

POM has a 9_5 helix conformation and packs in a hexagonal unit cell. The most intense diffraction is obtained from the close-packed $\{1\,0\,\bar{1}\,0\}$ planes, the $\{1\,0\,\bar{1}\,5\}$ planes giving the second strongest diffraction. These two sets of planes were used for the X-ray investigation.

Chang *et al.* [5] managed to obtain a (0 0 0 9) pole figure from a very highly oriented POM

sample. Even so the pole figure contained 'a "ghost" from the neighbouring $(1\,1\,\bar{2}\,5)$ poles'. This is not surprising since Carazzolo [25] states that the relative intensity of the $1\,1\,\bar{2}\,5$ to 0009 reflections is 20 : 1, whereas the respective values of 2θ for Cu$K\alpha$ radiation are 48.3° and 47.1°. The crystal thickness perpendicular to the 0009 planes is only about 150 Å; the consequent broadening of the 0009 diffraction will prevent it from being separated from the $1\,1\,\bar{2}\,5$ diffraction peak. 0009 pole figures will be at best qualitative, if the orientation is strong enough to know which peaks to disregard. In the event the intensity found at a Bragg angle of $2\theta = 47°$ was indistinguishable from the background level, so no 0009 pole figures were produced.

Cubes of 1 mm side were cut from the rolled sheets for mounting in a goniometer. A four-circle diffractometer was used in which the scintillation counter was fixed and the specimen rotated on two perpendicular axes. Cu$K\alpha$ radiation from a Phillips PW310 X-ray generator was used. Measurements were made automatically over 5° intervals with a count time of 5 sec, and recorded on punched tape. A chart record of integrated intensity was also made. The background count rate was taken as the average of the count rates at two degrees either side of the Bragg angle.

The following computations were then made by computer: the background was subtracted from each count, and the counts were then averaged to give the value, I_{av}, which would have been the diffracted intensity for an isotropic specimen. Contours of the diffracted intensity at levels of $I_{av}/2$, I_{av}, $2I_{av}$, $4I_{av}$, etc. were calculated by interpolation between the three nearest points plotted on a stereographic projection, and labelled 1, 2, 3, 4, etc. respectively.

5.2. Stresses and dimensions in uniaxial rolling

In order to estimate the stresses in the rolling of POM, plane strain compression tests were made using apparatus similar to that described by Williams and Ford [26]. The strain-rate of approximately 10^{-2} min^{-1} is about 10^{-3} of that in the rolling process, and the increments of plastic strain were somewhat larger, but an approximate value of the stresses in the rolling can be obtained. The die breadth used was 6.2 mm, and sheet of 6 mm thickness and 30 mm width was tested. These dimensions ensure that uniform plane strain

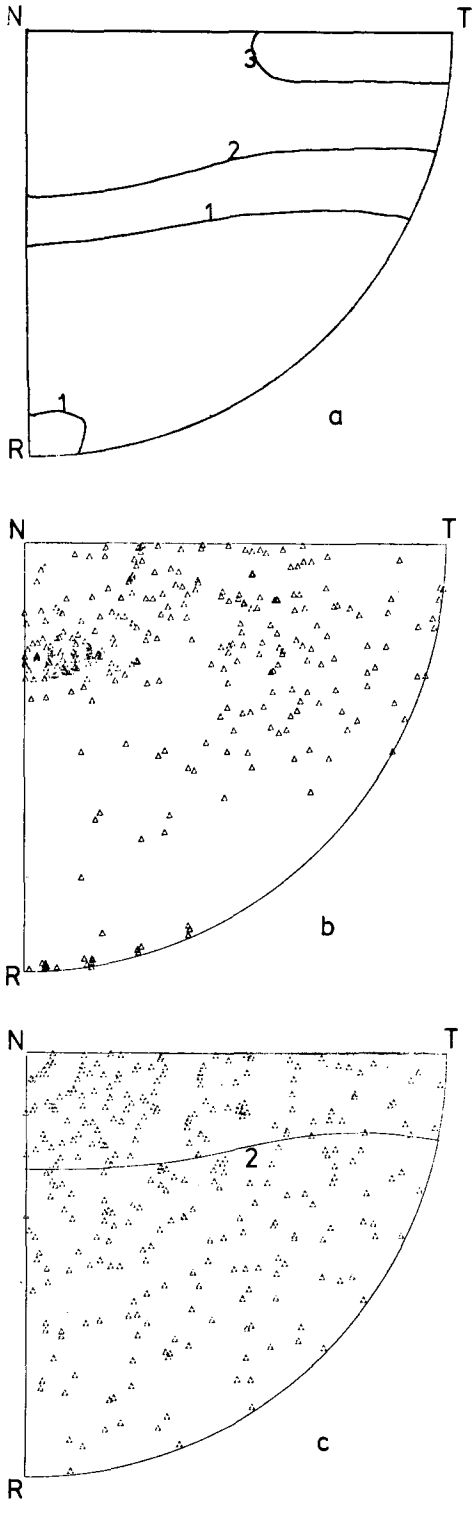

Figure 8 Comparison of experimental and theoretical $1\,0\,\bar{1}\,0$ pole figures for POM uniaxially rolled to $r = 0.7$. (a) experimental; (b) crystal slip; (c) Wilchinsky. Contour levels in (a) and (c) are the same as in Fig. 2. (c) shows separately the predictions for a discrete set of 99 crystals, and the contours of a continuous pole distribution.

deformation occurs between the dies. In an attempt to achieve larger plastic strains, some POM was plane strain compressed in a channel, in a device similar to that used by Chin and Nesbitt [27].

The length, width and thickness of a rectangular POM sheet (90 mm x 90 mm x 6 mm) were measured at several positions during uniaxial rolling.

6. Experimental results

6.1. Pole figures for uniaxially rolled POM

Fig. 8a shows the experimental $1\,0\,\bar{1}\,0$ pole figure for a uniaxially rolled POM sheet with a thickness reproduction $r = 0.7$. Only one quadrant is shown since the pole figure had mirror symmetry about the *RN* and *TN* planes. Figs. 8b and c show the predictions of the crystal slip and Wilchinsky model, respectively. They both predict an increased intensity band running from *N* to *T*, but the overall variation in intensity in the Wilchinsky prediction is less than the experimental variation. The crystal slip model is better in this respect; it also predicts intensity peaks at *R* and 30° from *N* in the *NR* plane, the former of which is observed and the latter may be present but swamped in the intensity band from *N* to *T*. There was little variation from uniform intensity in either the experimental or theoretical $1\,0\,\bar{1}\,5$ pole figures, so these are not shown.

Fig. 9 shows $1\,0\,\bar{1}\,0$ and $1\,0\,\bar{1}\,5$ pole figures at a thickness reduction $r = 0.5$. The experimental $1\,0\,\bar{1}\,0$ pole figure now has an intensity minimum at *N*, and maxima at *R*, *T*, and 30° from *N* in the *NR* plane. Preedy and Wheeler [4] have published an almost identical pole figure. Those of Gezovich and Geil [1] are fairly similar, but there is a strong possibility that their starting material did not have a fully spherulitic microstructure. The crystal slip model (Fig. 9b) predicts the features of the $1\,0\,\bar{1}\,0$ pole figure with the exception of the peak at *T*. The Wilchinsky model (Fig. 9c) is much less successful, being wrong in its predictions at *R*, *T* and *N*. The experimental $1\,0\,\bar{1}\,5$ pole figure has only the beginnings of a peak 40° from *R* in the *RT* plane. Gezovich and Geil find a similar feature, but also have a small peak at *N*. Neither of the computed $1\,0\,\bar{1}\,5$ pole figures show any high intensity regions, only a weakening of intensity from *N* to *T*, and at *R*. They disagree with the experimental figure but not strongly.

At a thickness reduction of $r = 0.3$ the experimental $1\,0\,\bar{1}\,0$ figure (Fig. 10a) has a strong intensity band from *N* to *T*, with a subsidiary peak 30° from *N* in the *RN* plane. There is a weak peak at *R* visible on the diffractometer trace but it falls below the 1 level. The $1\,0\,\bar{1}\,5$ pole figure has a broad band of increased intensity approximately 40° from *R*, with a maximum in the *RT* plane. If the Wilchinsky model distribution (Figs. 2c, 10c and f) is rotated by $\pi/2$ about *N*, this almost exactly matches the experimental intensity contours, apart from the small element of $\{1\,\bar{2}\,1\,0\}$ $\langle 1\,0\,\bar{1}\,0\rangle$ texture. This would be a $0\,0\,0\,1$ distribution peaking at *R* and falling off more rapidly away from the *RN* plane than in it, with Euler angle γ randomly distributed. The Wilchinsky model fails to predict the textures correctly. The crystal slip model (Fig. 10b and e) is better, but the pole distributions are too sharply peaked, and the element of $\{1\,\bar{2}\,1\,0\}$ $\langle 1\,0\,\bar{1}\,0\rangle$ texture is too strong.

On the basis of wide-angle X-ray diffraction data, we cannot agree with the conclusion of Gezovich and Geil that severe structural changes occur at a rolling reduction of about 0.4. There appears to be a continuous development of the textural features, with the exception of the reduction in the $\{1\,\bar{2}\,1\,0\}$ $\langle 1\,0\,\bar{1}\,0\rangle$ texture at $r = 0.3$.

6.2. Pole figures for biaxially rolled POM

At a thickness of 0.5, the $1\,0\,\bar{1}\,0$ pole figure from equally biaxially rolled POM (Fig. 11a) shows peaks at R_1, R_2 and at 45° from *N* midway between R_1 and R_2. The $1\,0\,\bar{1}\,5$ pole figure is less varied, with slight maxima near *N* and midway between R_1 and R_2. Gezovich and Geil have published similar pole figures. The Wilchinsky model for each biaxial rolling predicts pole figures that are axially symmetric about *N*, and Fig. 7 shows that the $1\,0\,\bar{1}\,0$ pole figure should peak at *N*, falling below the 3-level about 16° from *N*, and that the $1\,0\,\bar{1}\,5$ pole figure should peak about 55° from *N*. Subsequent rolling reduction would only intensify the peaks without changing their positions, so that the Wilchinsky model is at variance with the biaxial rolling results. The crystal slip model predicts peaks in the $1\,0\,\bar{1}\,0$ pole figure around the R_1R_2 plane and at about 30° from *N*, whereas the $1\,0\,\bar{1}\,5$ figure has a slight increase in peripheral pole intensity, and a decrease at *N*.

Biaxial rolling is possible to greater reductions than uniaxial rolling, and Fig. 12 shows pole

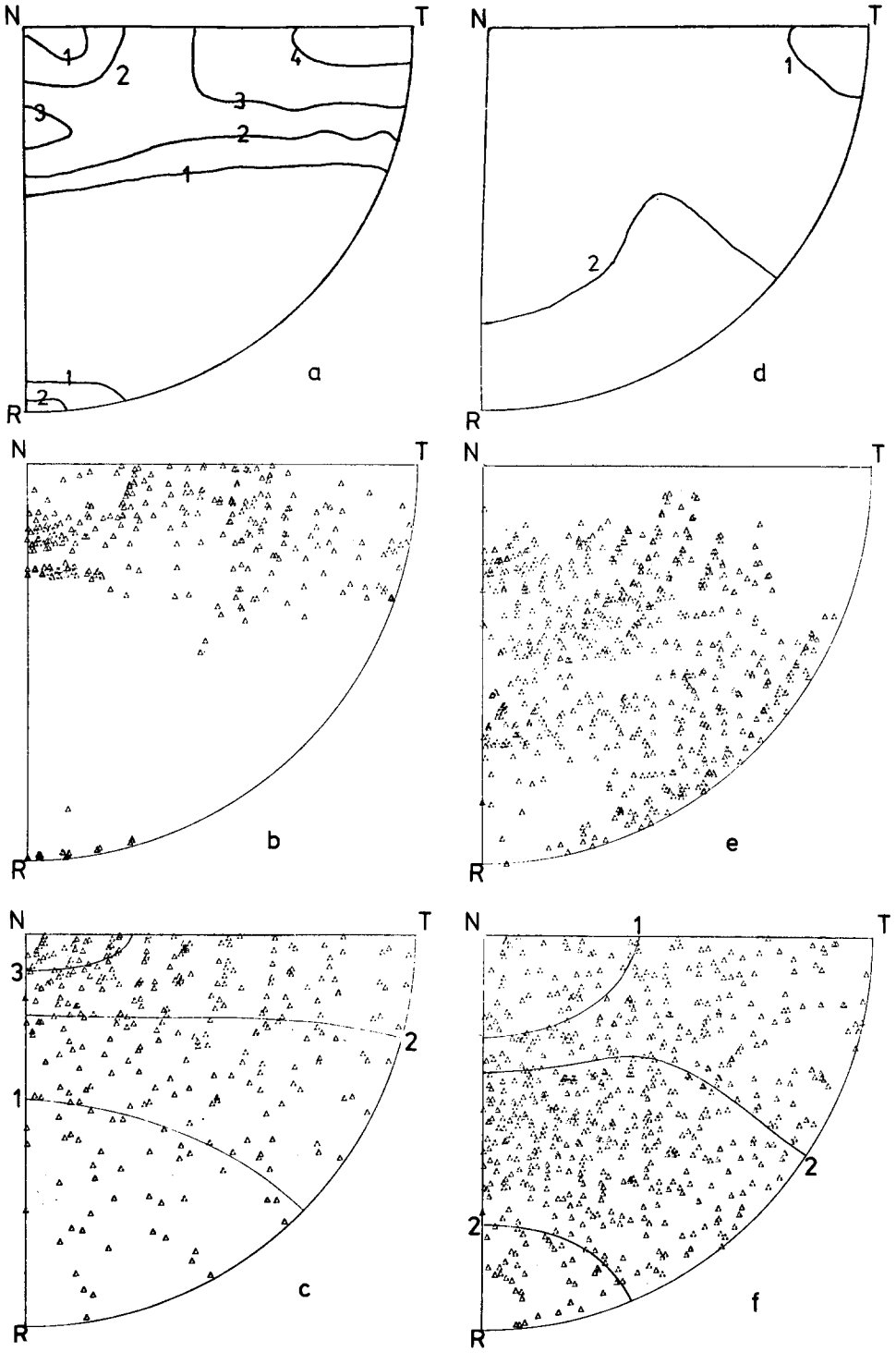

Figure 9 Comparison of $1\,0\,\bar{1}\,0$ and $1\,0\,\bar{1}\,5$ pole figures for POM uniaxially rolled to $r = 0.5$. (a) is the experimental $1\,0\,\bar{1}\,0$, (b) the crystal slip $1\,0\,\bar{1}\,0$, (c) the Wilchinsky $1\,0\,\bar{1}\,0$, (d) the experimental $1\,0\,\bar{1}\,5$, (e) the crystal slip $1\,0\,\bar{1}\,5$, and (f) the Wilchinsky $1\,0\,\bar{1}\,5$.

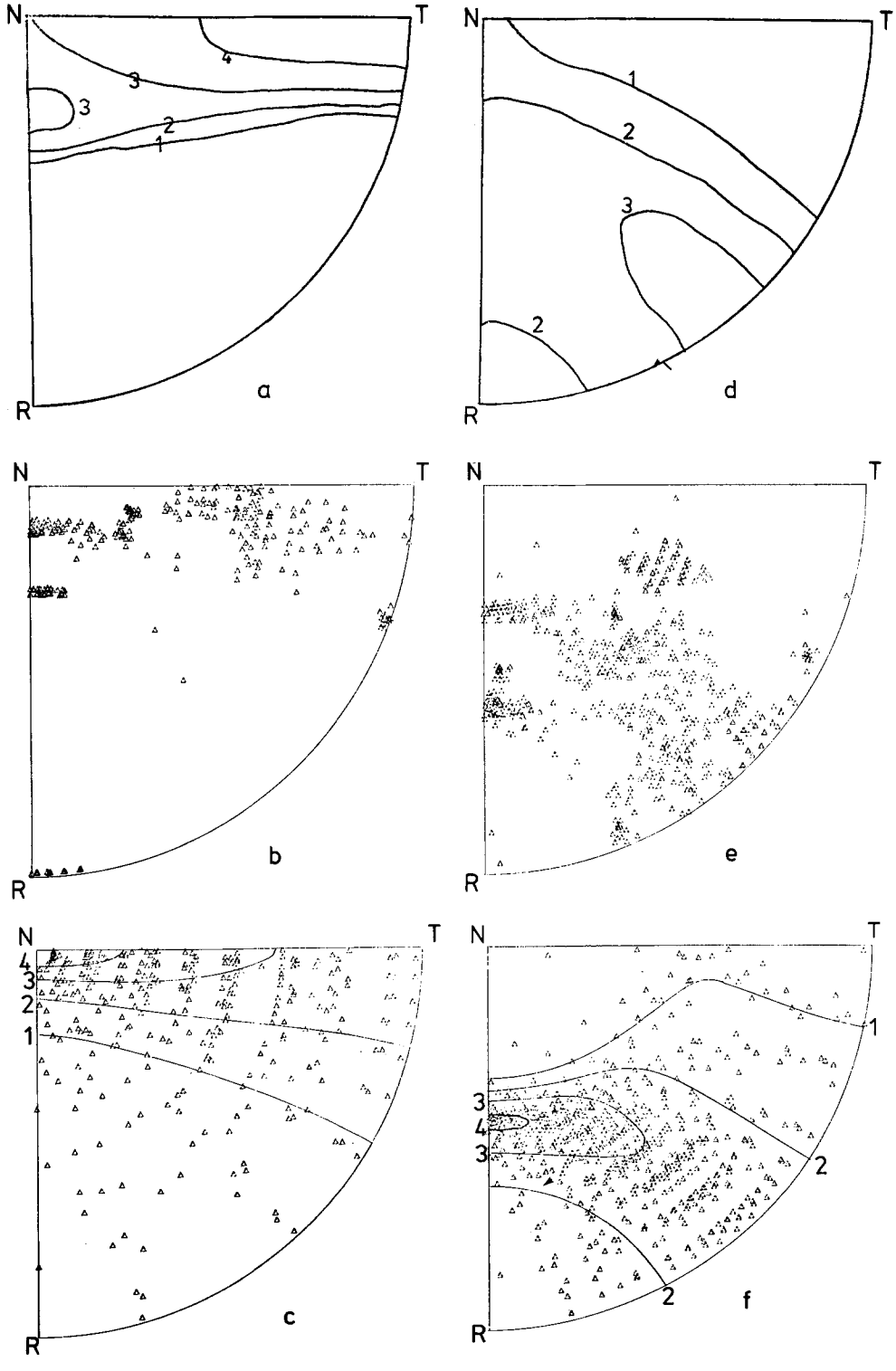

Figure 10 As for Fig. 9 except $r = 0.3$.

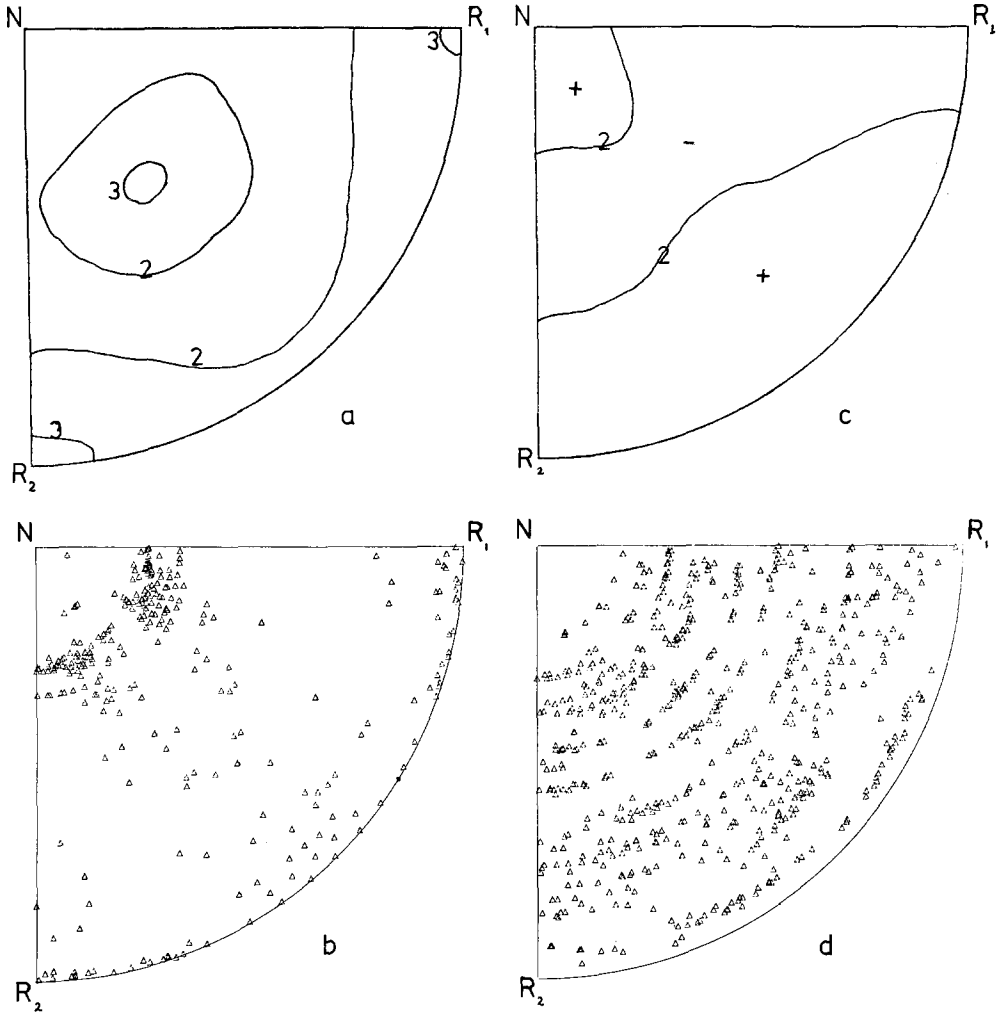

Figure 11 Comparison of experimental and theoretical $1\,0\,\bar{1}\,0$ and $1\,0\,\bar{1}\,5$ pole figures for POM equally biaxially rolled to $r = 0.5$. (a) is the experimental $1\,0\,\bar{1}\,0$, (b) the crystal slip $1\,0\,\bar{1}\,0$, (c) is the experimental $1\,0\,\bar{1}\,5$, and (d) the crystal slip $1\,0\,\bar{1}\,5$.

figures for $r = 0.13$. The peaks in the $1\,0\,\bar{1}\,0$ pole figure at R_1 and R_2 are sharper, and the remaining peak has moved in to within 40° of N. In the $1\,0\,\bar{1}\,5$ pole figure most of the intensity is towards the periphery. The crystal slip model predicts three features, $\{1\,\bar{2}\,1\,0\}\ \langle 1\,0\,\bar{1}\,0\rangle$ textures with respect to both R_1 and R_2, and a component described by the Euler angles $\alpha = 45°$, $\beta = 80°$, and γ random. It is this last component which does not appear to be present experimentally. In general, it can be said that the crystal slip model is far superior to the Wilchinsky model in predicting biaxial rolling textures, however, in detail it is not perfect. The clustering of the $0\,0\,0\,1$ poles about R_1 and R_2 must be somewhat different, and it is unlikely that many $0\,0\,0\,1$ poles can balance precariously at a midway position. However, it is not feasible to interpret the pole figures in terms of the distribution described by Gezovich and Geil, i.e. $\alpha = 0$ and $\pi/2$, $\beta = \pi/3$, and γ random.

6.3. Stresses and dimensions in uniaxial rolling

The results of the plane strain compression tests at 20° C are shown in Fig. 5. The initial yield stress was $127\,\mathrm{MN\,m^{-2}}$, and it can be seen that the slope of the true stress–strain curve increases with increasing strain. Plane strain compression tests in a rectangular channel were terminated by the specimen fracturing into a number of pieces at a compressive stress of $307\,\mathrm{MN\,m^{-2}}$ and a true thickness strain of -1.55. Thus it is unlikely that thickness reduction ratios much less than 0.3 can be achieved by uniaxially rolling. A rough estimate

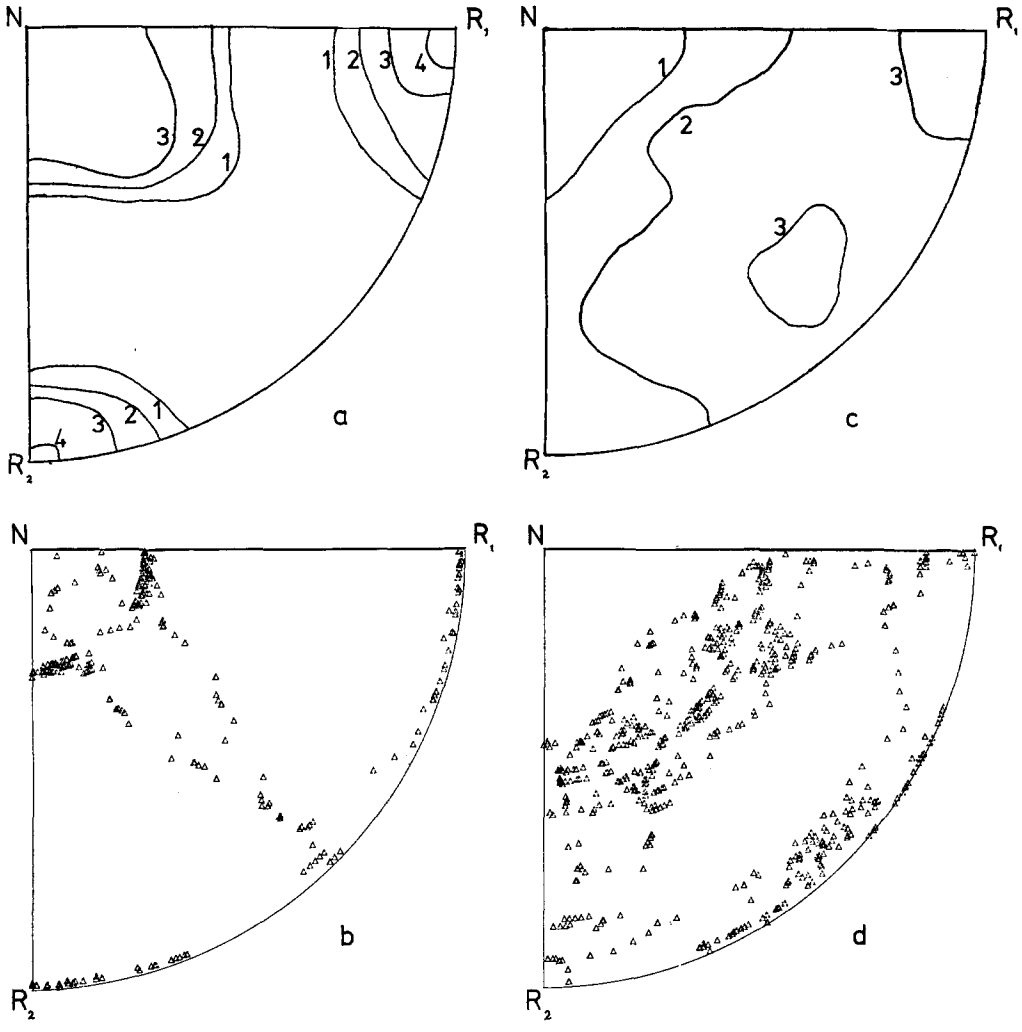

Figure 12 As Fig. 11 except $r = 0.13$ experimental and $r = 0.2$ crystal slip model.

of the critical resolved shear stress for prism slip may be obtained by dividing the experimental yield stress by 2 to obtain the deviatoric stress in the N direction, and by 1.22 (the theoretical initial ratio of the deviatoric stress to the resolved shear stress). The result is 52 MN m^{-2}.

During uniaxial rolling the plastic strain in the width direction was 6% at $r = 0.5$, rising to 11% at $r = 0.3$. Initially, the sheet became less opaque, and its density by about 0.2% at a thickness reduction of 0.5. By a reduction of 0.3 the appearance had become silvery, and the density had returned to its initial value. Cracks tended to grow in from the sheet edges, with crack plane perpendicular to R. It is suspected that the silvery appearance, and relative density decrease are a result of internal microvoiding.

6.4. Evidence for an orthorhombic phase

Carazzola and Mammi [28] found that POM polymerized with certain catalysts is obtained with an orthorhombic cell, and that this form reverts to the hexagonal form at 60° C. Preedy and Wheeler [4] have suggested that the pole figures such as Fig. 9a represent an orthorhombic (0 1 0) [0 0 1] texture, giving strong (0 2 0) pole figure maxima at T and a weaker maximum at N. Chang *et al.* [5] commented that the X-ray diffraction data of Preedy and Wheeler are insufficient evidence for the orthorhombic phase, since in conventional POM sheet the crystallite size is small and hence the $(1\,0\,\bar{1}\,0)$ diffraction from the hexagonal unit cell is broad and covers the positions of the (1 1 0) and (0 2 0) diffraction peaks from any orthorhombic phase. If the orthor-

hombic form were produced by rolling, thermal analysis should reveal its presence. Therefore, a 20 mg sample of the $r = 0.5$ uniaxially rolled POM sheet was examined in a Perkin Elmer Differential Scanning Calorimeter Model 2. The specific heat–temperature relation was determined at a heating rate of 20° C min^{-1}. There was a smooth increase in specific heat from 40 to over 120° C, thus ruling out the initial presence of any orthorhombic phase.

7. Discussion

On the basis of comparison of experimental and predicted pole figures for rolled POM, a crystal slip deformation mechanism seems to be closer to the real situation for POM than the Wilchinsky model of rigid crystals rotating. However, in order to be able to predict the rolling texture of POM, a great many assumptions had to be made. In the light of the results, the following comments can be made on the assumptions.

The development of an element of $\{\bar{1}\,2\,\bar{1}\,0\}$ $\langle 1\,0\,\bar{1}\,0\rangle$ texture in rolling is fairly good evidence for the operation of prism slip systems. However, confirmation of the slip systems by the observation of the deformation of POM in an electron microscope would be desirable. Another unknown is the extent and the nature (elastic or plastic) of the interlamellar shear. Perhaps the reason for the occurrence of voiding at rolling reductions $r \leqslant 0.3$ is that the limit of strain accommodation by interlamellar shear has been reached.

The problem of predicting the yield surface of POM from the texture, the yield behaviour of a single crystal, and the degree of crystallinity has hardly been touched on, yet it is needed for an analysis of the rolling process. All that can be concluded at this stage is that crystal reorientation is responsible for some but not all of the increase in the yield stress as rolling continues. Further analysis is needed of the onset of yielding in a uniformly stressed polycrystal, and of the variation in the plastic strain from crystal to crystal. It would seem likely that crystals can slip simultaneously on two or more slip systems. However, experimental evidence of such behaviour is required before adding to the complexity of the crystal slip model.

The examination of both the crystal slip model and the Wilchinsky model has shown that one crucial assumption is that of the constraints on a crystal in a deforming material. Wilchinsky presented his model as one in which the crystals are undeformed, but there is nothing in the model that prevents crystal slip from occurring. Similarly the assumption of uniform stress in the polycrystalline model is no guide to the selection of the constraints on the crystals. Thus what is required is a description of the constraints on a crystal that tallies with the observed development of textures. The constraints used in the crystal slip model are too precise, in that some variation in the amount of rotation is expected. The constraints in the Wilchinsky model are perhaps too imprecise, but it is the implications of a single reorientation mechanism that is the major drawback of the model. This becomes particularly obvious in the case of equal biaxial rolling, where the model predicts the same texture as for uniaxial compression. In a future paper we show that there is a great difference between the two experimental textures.

It would be an advantage at a future date to make use of low-angle X-ray data in a crystal slip model that incorporated the lamellar shape of the crystals. Also, since X-ray data can only present an average picture of the microstructure, the electron microscope could be used to attribute different deformation mechanisms to different regions of the spherulitic microstructure. At this stage it can only be concluded that a variety of crystal slip mechanisms play an important part in the development of texture in deformed POM.

8. Conclusions

(1) Pole figures have been calculated from Wilchinsky's model of crystal reorientation in rolling. Even accepting the weakly justified assumption that it is the 0 0 0 1 axes that reorient on deformation, it was not possible to obtain a good correspondence with observed pole figures.

(2) An analysis of the deformation of POM using the two most likely slip systems in the crystalline phase leads to a reasonable prediction of uniaxial and biaxial pole figures. It is, therefore, worthwhile to refine this model to include work hardening and other effects.

(3) The observation of a near perfect $\{1\,0\,\bar{1}\,0\}$ [0 0 0 1] texture in POM rolled at 126° C [5] cannot be explained by either of the above models. This suggests that other processes such as lamellar breakdown, or recrystallization come into play at elevated temperature.

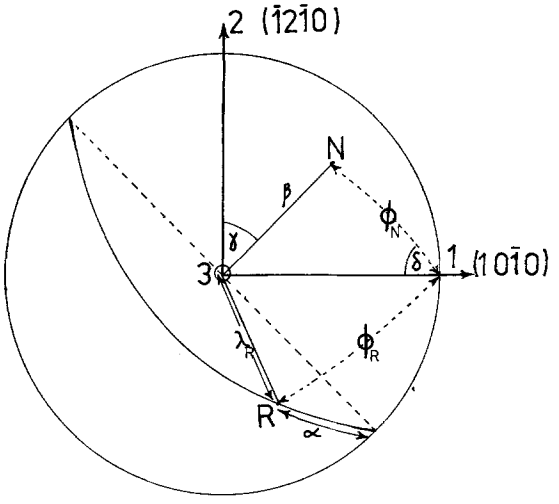

Figure 13 Perspective drawing of the upper surface of a unit sphere, showing the relationship of the *RTN* of the crystal 123 axes in terms of the Euler angles. The angles λ and ϕ for the slip system (1 0 1 0) [0 0 0 1], are also shown.

Appendix 1. Relation of the angles Φ and λ used in determining crystal rotations to the Euler angles

Fig. 13 shows the positions of N and R on the surface of a sphere in terms of the Euler angles. For the $(1\,0\,\bar{1}\,0)$ [0 0 0 1] slip system $\lambda_N = \beta$, and the other λ and ϕ angles between N or R and the slip direction and slip plane normal, respectively, are shown. By considering spherical triangles the following relationships can be deduced

$$\cos\phi_N = \sin\beta\sin\gamma \quad \text{(triangle with side } \pi/2\text{)} \quad \text{(A1)}$$

$$\cos\phi_R = \cos\alpha\cos\gamma - \sin\alpha\sin\gamma\cos\beta \quad \text{(A2)}$$

$$\cos\lambda_R = \sin\alpha\sin\beta \quad \text{(triangle with side } \pi/2\text{)}. \quad \text{(A3)}$$

Once the new values ϕ'_N, λ'_R, λ'_N have been calculated, the new Euler angles can be found using

$$\beta' = \cos^{-1}(\cos\lambda'_N) \quad \text{(A4)}$$

$$\alpha' = \sin^{-1}(\cos\lambda'_R/\sin\beta'). \quad \text{(A5)}$$

The new value of γ can be found by using the fact that N moves on a great circle towards the slip plane normal $1\,0\,\bar{1}\,0$, so the angle δ is a constant. Now

$$\sin\delta = \sin\beta\cos\gamma/\sin\phi_N = \sin\beta'\cos\gamma'/\sin\phi'_N$$

so

$$\sin\beta'\cos\gamma' = r\sin\beta\cos\gamma$$

and

$$\gamma' = \cos^{-1}(r\sin\beta\cos\gamma/\sin\beta'). \quad \text{(A6)}$$

For the slip systems 2 and 3, γ is replaced by $\gamma + \pi/3$ and $\gamma + 2\pi/3$, respectively, throughout.

For the prism slip system 4, Equations A1 and A2 above still hold, but now

$$\cos\lambda_N = \sin\beta\cos\gamma$$

and

$$-\cos\lambda_R = \cos\alpha\sin\gamma + \sin\alpha\cos\gamma\cos\beta.$$

β' and γ' are recovered by equations A4 and A6, but now

$$\alpha' = \sin^{-1}(\sin\alpha\sin\beta/L\sin\beta').$$

Again for systems 5 and 6 $\gamma + \pi/3$ and $\gamma + 2\pi/3$ are substituted for γ throughout.

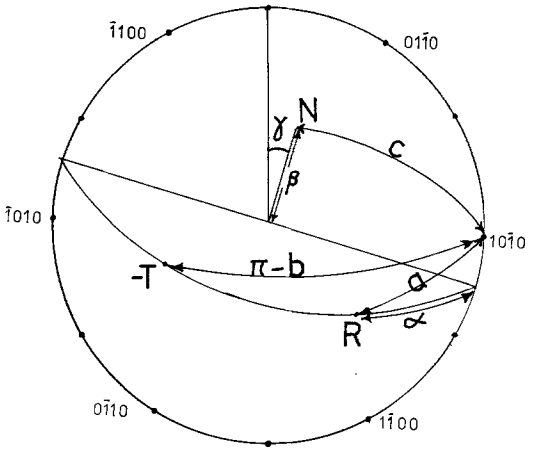

Figure 14 As Fig. 13, showing the angles used in the recovery of the co-ordinates of the $1\,0\,\bar{1}\,0$ poles from the Euler angles.

Appendix 2. Recovery of pole figures

Recovery of the 0 0 0 1 pole figure is straightforward, since the pole position is defined by α' and β'. Recovery of the $1\,0\,\bar{1}\,0$ pole figure is a little more complex, since there are three $1\,0\,\bar{1}\,0$ poles for each crystal. Fig. 14 shows that the angular distances of interest (a, b, and c) are those of R, T and N from a typical $1\,0\,\bar{1}\,0$ pole. Defining the angle $G = \gamma + (n-1)\pi/3$ $n = 1, \ldots, 5$ then the distance of the pole from N is

$$\cos c = \sin\beta\sin G.$$

If poles having $\cos c < 0$ are rejected then the remaining poles lie with $\pi/2$ of the centre of the stereographic projection at N. The angular distances a and b are given by

$$\cos a = \cos\alpha\cos G - \sin\alpha\sin G\cos\beta$$

$$\cos b = \sin\alpha\cos G + \cos\alpha\sin G\cos\beta.$$

From these, the Cartesian coordinates of the poles in the $1\,0\,\bar{1}\,0$ pole figure are $(x, -y)$ where

$$x = |\cos b|/(1 + \cos c)$$

$$y = |\cos a|/(1 + \cos c).$$

Use of the absolute values of $\cos a$ and $\cos b$ reflects the three poles about the *NT* or *NR* planes into the fourth quadrant.

The recovery procedures for the $1\,0\,\bar{1}\,5$ pole figures are of a similar nature.

Acknowledgements

M. J. Miles is grateful to Professor R. E. Smallman for arranging financial support. We would like to thank Dr. W. B. Hutchinson for many helpful discussions.

References

1. D. M. GEZOVICH and P. H. GEIL, *J. Mater. Sci.* **6** (1971) 509.
2. E. S. CLARK, *S.P.E. J.* **23** (1967) 46.
3. H. W. STARKWEATHER, F. C. WILSON and E. S. CLARK, *J. Polymer Sci. Letters* **9** (1971) 623.
4. J. E. PREEDY and E. J. WHEELER, *Nature Phys. Sci.* **60** (1972) 236.
5. E. P. CHANG, R. W. GRAY and N. G. McCRUM, *J. Mater. Sci.* 8 (1973) 397.
6. K. O'LEARY and P. H. GEIL, *J. Macromol. Sci. B* **2** (1968) 261.
7. E. A. CALNAN and C. J. B. CLEWS, *Phil. Mag.* **41** (1950) 1085.
8. R. VON MISES, *Z. Angew. Math. Mech.* 8 (1928) 161.
9. A. KELLY and G. W. GROVES, "Crystallography and Crystal Defects" (Longman, London, 1970) p. 185.
10. I. L. DILLAMORE and W. T. ROBERTS, *Acta Met.* **12** (1964) 281.
11. T. LEFFERS, *Phys. Stat. Sol.* **25** (1968) 337.
12. J. S. KALLEND and G. J. DAVIES, *Phil. Mag.* **25** (1972) 471.
13. J. F. W. BISHOP and R. HILL, *Phil. Mag.* **42** (1951) 414.
14. C. F. HAMMER, T. A. KOCH and J. F. WHITNEY, *J. Appl. Polymer Sci.* **1** (1959) 169.
15. Z. W. WILCHINSKY, *Polymer* **5** (1964) 271.
16. I. L. HAY and A. KELLER, *Kolloid-Z. u. Z. Polymere* **204** (1965) 43.
17. T. T. WANG, *J. Polymer Sci.* **12** (1974) 145.
18. D. C. BASSETT, *Phil. Mag.* **10** (1964) 595.
19. C. A. GARBER and P. H. GEIL, *Die Makromol. Chemie* **113** (1968) 251.
20. R. J. YOUNG, P. B. BOWDEN, J. M. RICHIE and J. G. RIDER, *J. Mater. Sci.* 8 (1973) 23.
21. J. SCHULTZ, "Polymer Materials Science" (Prentice Hall, New Jersey, 1974) p. 91.
22. J. D. ESHELBY and A. N. STROH, *Phil. Mag.* **42** (1951) 1401.
23. G. W. ROWE, "Principles of Metalworking" (Arnold, London, 1965) Ch. 9.
24. B. WUNDERLICH, "Macromolecular Physics", Vol. 1 (Academic Press, New York and London, 1973).
25. G. CARAZZOLA, *J. Polymer Sci. A* **1** (1963) 1573.
26. J. G. WILLIAMS and H. FORD, *J. Mech. Eng. Sci.* **6** (1964) 405.
27. G. Y. CHIN and E. A. NESBITT, *Trans. Amer. Inst. Min. Met. Petr. Eng.* **236** (1966) 69.
28. G. CARAZZOLA and M. MAMMI, *J. Polymer Sci.* **1** (1963) 965.

Received 26 March and accepted 5 June 1975.